World Electric Vehicle Journal

MDPI

Article

Estimation of Road Adhesion Coefficient Based on Camber Brush Model

Shupei Zhang, Hongcheng Zhu *, Haichao Zhou, Yixiang Chen and Yue Liu

School of Automotive and Traffic Engineering, Jiangsu University, Zhenjiang 212013, China
* Correspondence: 2222104021@stmail.ujs.edu.cn

Abstract: Electric vehicles, with their distinct power systems, weight distribution, and power control strategies compared to traditional vehicles, influence the pressure distribution in the tire contact area, thereby affecting the estimation of road adhesion coefficient. In electric vehicle research, tire adhesion coefficient serves as a measure of the frictional force between the vehicle and the road surface, directly impacting the vehicle's handling performance. The accurate estimation of the adhesion coefficient aids drivers in better understanding the vehicle's driving state. However, the existing brush models neglect differences in ground pressure distribution along the width direction of tires during tire camber, potentially leading to inaccuracies in adhesion coefficient estimation. This study proposes a camber brush tire model that considers the width-direction pressure distribution characteristics, aiming to enhance the accuracy of adhesion coefficient estimation under camber conditions. Experimental comparisons between the improved and original models reveal a significant enhancement in estimation precision. Consequently, the findings of this study provide valuable insights for deepening our understanding of tire camber dynamics and for designing control systems for electric vehicles, thereby improving vehicle stability and safety.

Keywords: tire camber; road adhesion coefficient; ground pressure distribution

Citation: Zhang, S.; Zhu, H.; Zhou, H.; Chen, Y.; Liu, Y. Estimation of Road Adhesion Coefficient Based on Camber Brush Model. *World Electr. Veh. J.* **2024**, *15*, 263. https://doi.org/10.3390/wevj15060263

Academic Editor: Paulo J. G. Pereirinha

Received: 9 April 2024
Revised: 16 May 2024
Accepted: 12 June 2024
Published: 17 June 2024

1. Introduction

Electric vehicles are a type of new energy vehicle that can reduce greenhouse gas emissions and alleviate the shortage of petroleum energy. With various countries and organizations announcing plans to reduce the production and sale of gasoline-powered vehicles, new energy vehicles are gradually becoming mainstream, with electric vehicles being the most popular type among them. Electric vehicles exhibit significant differences in tire adhesion coefficient estimation compared to traditional vehicles due to their unique power systems, weight distribution, and power control strategies [1]. The application of electric motors can result in different force or torque distributions exerted by the vehicle on the road surface, affecting the friction between the tires and the road and consequently influencing the estimation of the adhesion coefficient. Electric vehicles typically utilize battery packs as energy storage devices, and the weight and size distribution of these battery packs differ from traditional fuel tanks, leading to distinct weight distribution characteristics in electric vehicles that affect the pressure distribution of tires on the road surface. The flexible power control strategies of electric vehicles, such as motor torque adjustment and energy recovery functions, can alter the power output patterns of the vehicle under different driving conditions, thereby affecting the friction between the tires and the road surface and consequently influencing the estimation of the adhesion coefficient. The accurate estimation of tire–road adhesion coefficient is of paramount importance for overall vehicle stability and safety. The precise estimation of adhesion coefficient aids drivers in better understanding vehicle dynamics across diverse road surfaces and driving conditions, thereby enhancing driver control. By comprehending the friction between tires and road surfaces, drivers can adeptly adjust driving strategies, minimizing the occurrence of accidents. Furthermore, the precise

estimation of adhesion coefficient furnishes accurate input parameters for vehicle dynamic stability control systems, facilitating the optimal adjustment of vehicle suspension, braking, and traction systems, thereby improving overall vehicle stability and safety. Therefore, the accurate estimation of tire–road adhesion coefficient is crucial for enhancing vehicle driving performance, safety, and ride comfort [2]. Additionally, the energy-saving and environmentally friendly characteristics of electric vehicles are closely related to the tire adhesion coefficient. By optimizing the vehicle's power systems and control strategies, energy consumption on different road surfaces can be reduced, leading to lower energy consumption and carbon emissions, and thus promoting the development of sustainable transportation [3].

The tire serves as the sole means of transmitting interaction forces between the road surface and the vehicle [4], providing sufficient traction for the stable operation of the vehicle through the contact between the tire and the ground [5]. Tire camber can alter the ground characteristics between the tire and the road surface, and the adhesive performance between the tire and the road surface is influenced by factors such as tire material, tread pattern, road surface roughness, and tire–ground characteristics [6–11]. Therefore, a tire mechanics model capable of accurately describing the ground characteristics between the tire and the road surface under camber conditions is of great significance for tire development and research on tire adhesion performance.

The brush tire model assumes the tire carcass to be rigid and the tread surface to be a row of elastic bristles. Then, by analyzing the forces acting on the bristles during ground contact, the tire forces are determined [12]. Later, scholars began to study the mechanical properties of tires using the brush model. Building upon this, Fiala [13] proposed the Fiala tire model, which derived the relationship between slip angle, lateral force, and self-aligning torque. Frank [14], drawing upon Fiala's research, characterized the tire carcass as a beam subjected to bending after force application. A complex model was formulated to describe the mechanical properties of the bent beam, enabling an investigation into the effects of carcass deformation on tire mechanical characteristics under camber conditions. Fancher P et al. [15], building upon the brush tire model, proposed the HSRI-NBS-I model, postulating that the bristles undergo lateral and longitudinal deformations under lateral and longitudinal forces. Subsequently, Pacejka and Bakker [16] introduced the widely utilized Magic Formula, an empirical model that fits tire test data using a combination of trigonometric functions. This model accurately describes the forces and moments experienced by the tire under various conditions.

In the early stages, scholars paid relatively little attention to the issue of tire camber, often combining the effects of camber with those of lateral deviation and suggesting that camber exacerbated the effects of lateral deviation [17]. Kuiper E [18], building upon the brush model, established the camber brush tire model, revealing the relationship between tire camber angle and ground contact patch length, contact patch width, and tire effective radius. Bai F [19] developed a ground pressure distribution model for lateral slip conditions considering tire width. However, this model did not accurately account for the shape of the ground pressure distribution across the tire width. As a result, it could not accurately describe the ground pressure distribution in the width direction of the tire under different camber conditions. Su X [20] established finite element models of tires with different tread patterns to study the ground characteristics of tires under steady-state rolling conditions and with tire camber angles. The study considered variations in ground pressure distribution while keeping the tire contact width constant. However, it was observed that the actual tire contact patch width changed significantly under tilting conditions. Han Y [21] established a ground pressure distribution model considering tire width under camber conditions. However, this model assumes that the ground contact pressure decays along the tire width direction with a proportional coefficient, without establishing the relationship between factors such as tire camber angle, inflation pressure, vertical load, and the variation in contact width.

In the current research on the mechanical characteristics of the tire–road contact area and the estimation of tire adhesion coefficient, several unresolved issues remain. Most studies assume that the vertical pressure distribution in the tire–road contact area is symmetrical [22–26], with limited exploration into the mechanical characteristics under tire camber conditions. However, during vehicle operation, tires inevitably experience camber angles. Under the influence of camber, the vertical pressure distribution on the tire becomes significantly asymmetrical, which greatly affects the mechanical characteristics of the tire contact area and consequently impacts the study of the adhesion coefficient.

Therefore, this study analyzes the contact characteristics of the tire under camber conditions by establishing a finite element model of the tire and constructing a two-dimensional ground pressure distribution model. Based on this, the assumption of the brush model that ignores the contact characteristics in the width direction is improved. Combined with a seven-degree-of-freedom vehicle model, an adhesion coefficient estimation algorithm is designed based on the extended Kalman filter to improve the accuracy of adhesion coefficient estimation under camber conditions.

2. Tire Finite Element Model

2.1. Finite Element Structural Model

Taking 205/55R16 radial tire as the research object, the cross-sectional profile of the tire was established using AutoCAD 2019. The complexity of the tread pattern complicates the meshing process in the model, resulting in difficulties in achieving convergence in simulation results. Research findings indicate that the tread pattern has minimal impact on the characteristics of ground contact patches as tire pressure and load vary [27]. Therefore, a longitudinal groove tread pattern model was adopted for subsequent ground contact simulations.

The geometric modeling is imported into HyperMesh 2019 for geometric cleaning and mesh generation. Subsequently, an "INP" file containing all tire model information is exported. In the simulation, rubber materials are represented using CGAX3H (three-node general linear axisymmetric triangular shell element) and CGAX4H (four-node general bilinear axisymmetric quadrilateral shell element) elements, while the reinforcement is modeled using SFMGAX1 (two-node linear axisymmetric curved surface element) elements and carried out with the rebar layer [28]. To embed the reinforcement layer into the rubber matrix, embedded element constraints are employed.

Subsequently, the corresponding material properties are assigned to the cross-section of each component of the tire. The stress–strain relationship of the rubber material is described using the Neo-Hookean constitutive model, while the reinforcement is modeled to simulate fiber-reinforced material. Specific material parameters can be found in [29]. The two-dimensional finite element model is illustrated in Figure 1a.

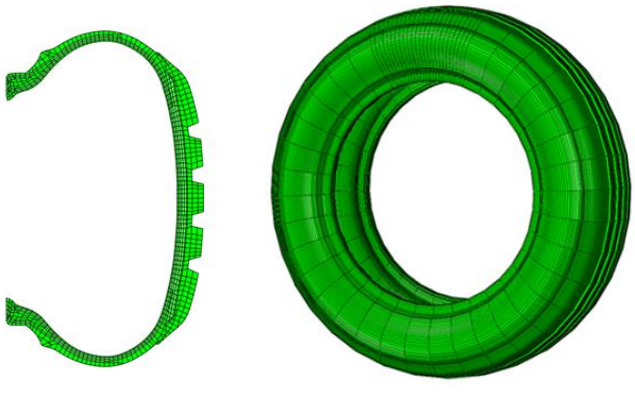

(**a**) (**b**)

Figure 1. (**a**) Two-dimensional tire finite element model. (**b**) Three-dimensional tire finite element model.

In ABAQUS/Standard, the keyword *SYMMETRIC MODEL generalization is utilized to generate the three-dimensional finite element model of the tire. To accelerate computation speed and ensure accuracy, mesh refinement is only required in the contact area, as illustrated in Figure 1b. The tire rim and road surface are designated as analytical rigid bodies. Relative motion between the tire and rim is neglected. Finally, Coulomb friction is employed as the friction model between the tire and the road surface.

2.2. Verification of Finite Element Model

2.2.1. Mechanical Properties of Tire Materials

In the Abaqus simulation process, composite material structures are often defined using rebar elements. Material properties of cord elements are defined first, and then, these cord elements are embedded into the corresponding rubber solid elements. Therefore, the radial tire belt with cord layer rubber adopts the Yeoh model to describe its mechanical properties, and the material parameters of the internal cord rebar are shown in Table 1.

Table 1. Tire cord material parameters for each part.

Part	Density ($t \cdot mm^{-3}$)	Young's Modulus (Mpa)	Poisson's Ratio	Cross-Sectional Area (mm^2)	Ply Angle (°)
Carcass Ply	1.5×10^{-9}	10,539	0.4	0.21	90
Belt Ply 1	7.8×10^{-9}	205,251	0.3	0.27	67
Belt Ply 2	7.8×10^{-9}	205,251	0.3	0.27	113
Steel Bead	7.8×10^{-9}	210,000	0.3	1.31	0
Tread Ply	1.1×10^{-9}	2230	0.4	0.33	0

2.2.2. Grounding Footprint Verification

Grounding footprint verification is one of the commonly used methods to validate the accuracy of tire finite element models. To validate the accuracy of the finite element model and ensure simulation precision, a static ground contact test on the tire is conducted using the Tire Multifunction Testing Machine-2 (Guangdong, China). The tire is loaded to its rated load of 4821 N and rated pressure of 240 kPa. In the static ground contact test, ink imprints are used to obtain ground contact patches, from which geometric parameters are extracted.

Figure 2 illustrates the ground contact imprints from both the static ground contact test and the finite element analysis, and the geometric parameters are listed in Table 2.

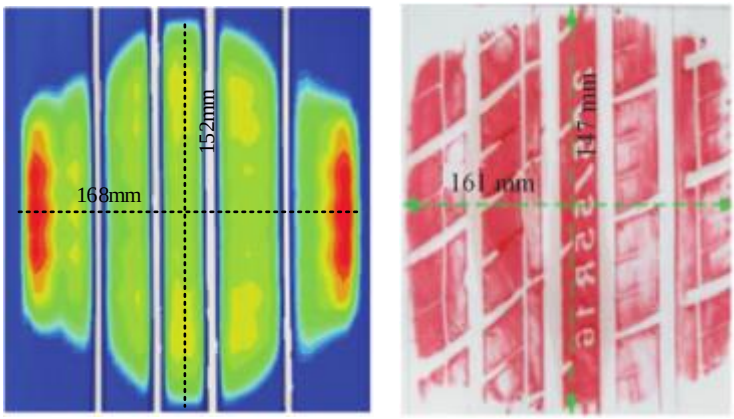

(**a**) (**b**)

Figure 2. Tire ground contact patch: (**a**) tire footprint obtained through the FEA and (**b**) tire footprint obtained through the experiment.

Table 2. Area characteristic parameters.

Solution	FEA	Experiment	Error
contact length/mm	152.08	147.13	3.36%
contact width/mm	168.75	161.05	4.78%

The finite element simulation results are in good agreement with the experimental results, with a maximum relative error of only 4.78% in contact length and width. This indicates that the established finite element model can accurately reflect the tire footprint on the ground.

2.2.3. Stiffness Verification

According to the test method specified in the national standard (GB/T 23663-2020), the stiffness of tire is evaluated using the MTM-2 machine. Simultaneously, the stiffness of the tire finite element model is simulated in ABAQUS, replicating the same conditions. The test results and simulation data are presented in Table 3.

Table 3. Comparison between simulation value and experiment value of tire stiffness.

Stiffness	FEA	Experiment	Error
radial stiffness/(N/mm)	212.94	206.28	3.23%
lateral stiffness/(N/mm)	88.76	92.62	4.17%
longitudinal stiffness/(N/mm)	133.77	137.99	3.06%

The tire stiffness obtained from experimental testing is compared with that derived from finite element analysis, both showing errors within 5%. This indicates that the established tire finite element model exhibits high accuracy in terms of tire stiffness. The validation results of ground contact imprint and stiffness analysis provide strong support for the high effectiveness of the tire finite element model developed in this study.

3. The Camber Brush Tire Model Considering Tire Width Effect

3.1. Simulation and Modeling of Tire Ground Contact Characteristics under Tire Camber

The influence of tire camber on the ground contact characteristics in the width direction of the tire is mainly reflected in two aspects: the width of the ground imprint and the pressure distribution along the width direction. The tire contact situation under tire camber conditions is shown in Figure 3. The coordinate origin in the diagram is located at the center of the contact patch, with the z-axis pointing upwards perpendicular to the ground, and the y-axis in the direction of tire width. $2b_0$ represents the contact width under steady rolling of the tire, $2b$ represents the contact width after tire camber, and $2a$ represents the length of the contact patch. As tire camber angle increases, the width of the contact patch significantly decreases, and the pressure distribution across the width, as shown by the shaded area in Figure 3, concentrates towards the direction of tire camber.

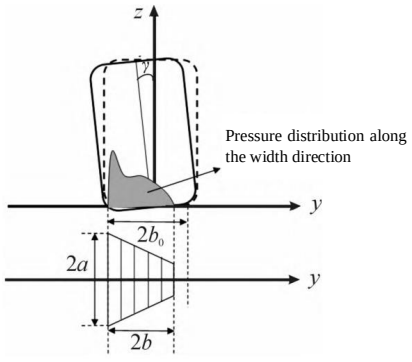

Figure 3. Tire ground contact illustration under camber.

Figure 4 illustrates the variation in contact patch width under different loads and inflation pressures with tire camber. The trend indicates that, as the camber angle increases, the width decreases. Additionally, under different inflation pressures, there is a notable rapid decrease in width at a certain camber angle. This phenomenon primarily occurs because the increased camber angle places the longitudinal grooves on the tire surface at the edge of contact. Moreover, with a constant tire load, higher inflation pressure results in smaller contact patch width values. Conversely, with constant inflation pressure, higher loads lead to larger width values.

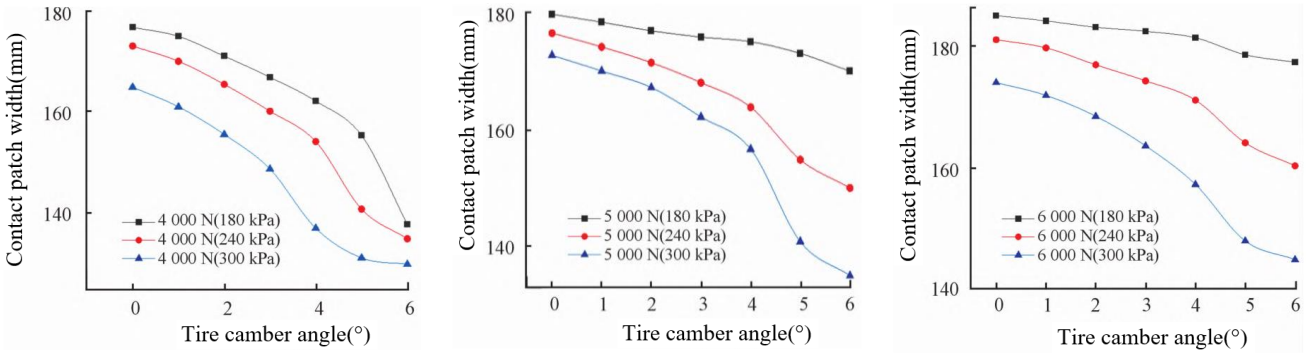

Figure 4. The width of the contact patch under different loads and tire pressures: (**a**) the distribution of ground pressure under a load of 4000 N, (**b**) the distribution of ground pressure under a load of 5000 N, and (**c**) the distribution of ground pressure under a load of 6000 N.

The tire contact patch width is inversely proportional to the inflation pressure and directly proportional to the load. Therefore, an exponential function is employed to fit the variation pattern of the contact patch width. The expression for the half-width b of the contact patch as it varies with load, inflation pressure, and camber angle is given by the following:

$$2b = 2b_0 - b_1 \frac{F_2^{b_2}}{P^{b_3}} \gamma \quad (1)$$

where b is the half-width of the tire contact patch, b_0 is the half-width of the contact patch under steady rolling conditions, b_1 is the coefficient of the half-width of the contact patch under steady conditions, b_2 is the coefficient of the half-width of the contact patch with respect to the load under steady conditions, b_3 is the coefficient of the half-width of the contact patch with respect to the tire pressure under steady conditions, and γ represents the camber angle.

To facilitate the extraction of pressure distribution data from the simulation results, seven paths parallel to the length of the tire contact patch are established in the tire contact area, as shown in Figure 5. The selection of paths is based on the division of the longitudinal grooves in the tire tread model into five sections, ensuring equal spacing between adjacent paths as much as possible. By analyzing the distribution of the sum of pressures along each path, the pressure distribution pattern in the width direction of the entire contact area can be approximated.

Figure 6 illustrates the pressure distribution in the width direction of the tire footprint under a load of 4000 N and inflation pressures of 180, 240, and 300 kPa, respectively. When the camber angle is 0°, the ground pressure distribution is generally symmetrical, with higher pressures observed in both shoulder areas and the middle region of the footprint width. As the camber angle increases, the pressure distribution shifts towards the direction of tire camber, concentrating towards the shoulder areas. However, with the increase in inflation pressure, there is a mitigating effect on the widespread distribution of ground pressure.

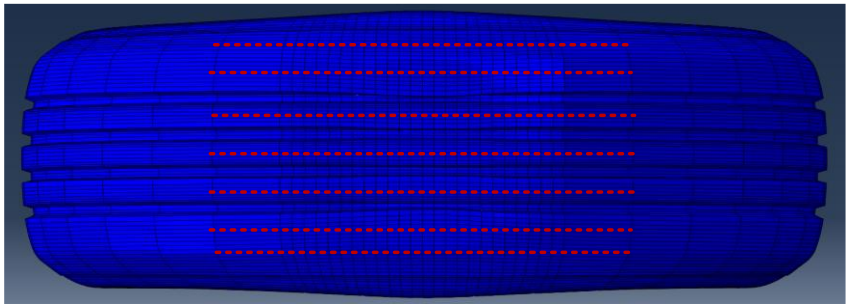

Figure 5. Seven paths on the tire tread area.

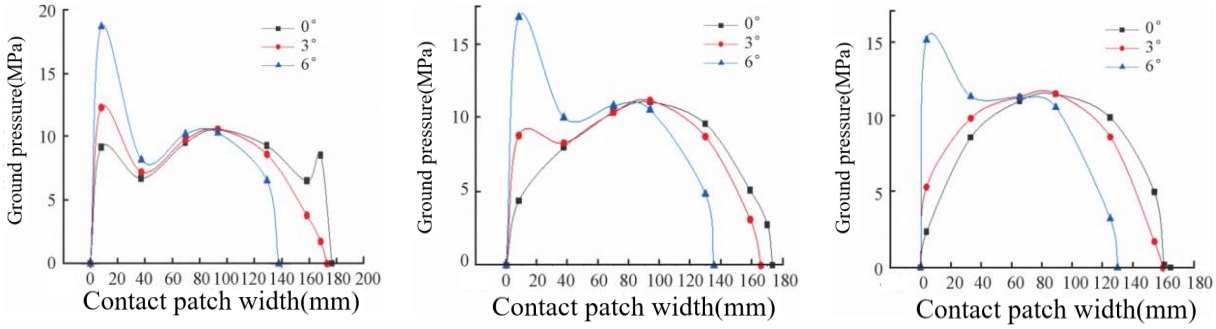

Figure 6. Ground pressure distribution under different inflation pressures at 4000 N: (**a**) ground pressure distribution at 180 kPa, (**b**) ground pressure distribution at 240 kPa, and (**c**) ground pressure distribution at 300 kPa.

Due to the significant variation in the contact patch with increasing camber angle, the width was normalized to visually analyze the pressure distribution. Additionally, a controlled variable analysis method was employed to further explore the effects of load, tire pressure, and camber angle on the ground pressure distribution. Pressure distributions along the width of the contact patch were plotted for different tire pressures at the same load and for different loads at the same tire pressure, with a camber angle of 0°, as shown in Figure 7. It can be observed that, at the same load, higher tire pressure results in a more pronounced upward convex trend in the pressure distribution. Similarly, at the same tire pressure, increasing load reduces the upward convex trend in the pressure distribution.

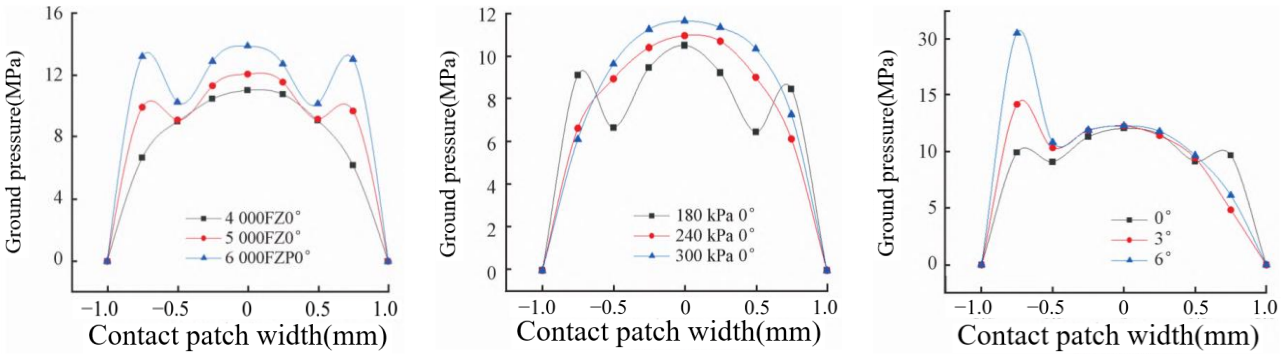

Figure 7. Concavity–convexity and biased characteristics of ground pressure distribution under normalized width: (**a**) ground pressure distribution under different loads, (**b**) ground pressure distribution under inflation pressure, and (**c**) ground pressure distribution under tire camber angle.

Based on the two-dimensional ground pressure model, a model for the characteristics of ground pressure distribution under camber conditions is established. The expressions for the pressure distribution models $Q_{zy}(y)$ and $Q_{zx}(x,y)$ are as follows:

$$Q_{zy}(y) = \frac{F_Z}{2b}\eta_y(y) \tag{2}$$

$$Q_{zx}(x,y) = \frac{q_{zy}}{2a}\eta_x(x) \tag{3}$$

$$v = \frac{y}{b} \tag{4}$$

$$Q_{zy}(v) = \frac{F_Z}{2b}\eta_y(v) \tag{5}$$

$$\eta_y(v) = A_y\left(1-v^2\right)\left(1+\lambda_y v^2\right)(1-B_y v) \tag{6}$$

$$A_y = \frac{15}{2(5+\lambda_y)} \tag{7}$$

$$B_y = \frac{7(5+\lambda_y)}{7+3\lambda_y}\frac{\Delta_y}{b} \tag{8}$$

where a is the half-length of the ground contact patch, b is the half-width of the contact patch, v is the relative position coordinate in the width direction, $\eta_y(y)$ and $\eta_x(x)$ are the pressure distributions in the width and length directions, respectively, λ_y is the concavity–convexity factor in the width direction, Δ_y is the bias factor in the width direction, and x and y are arbitrary positions in the length and width, respectively.

According to Figure 7, as the load increases, the distribution of ground pressure becomes more concave, i.e., the value of λ_y increases, and it shows a linear relationship with the load. With the increase in tire pressure, the distribution of ground pressure tends to be more convex, i.e., the value of λ_y decreases, and it shows a basically linear decreasing relationship with the tire pressure. Therefore, the expression for the concavity–convexity factor is as follows:

$$\lambda_y = q_{y1}F_z + q_{y2}P + q_{y3} \tag{9}$$

where q_{y1} is the load coefficient of concavity–convexity factor in the width direction, q_{y2} is the tire pressure coefficient of concavity–convexity factor in the width direction, and q_{y3} is the constant coefficient of concavity–convexity factor in the width direction.

From Figure 7, it can be observed that the ground pressure distribution becomes more severe with the increase in the camber angle. Therefore, the expression for the bias factor is as follows:

$$\Delta_y = q_{y4}r^{q_y 5} \tag{10}$$

where q_{y4} and q_{y5} is the coefficient of bias factor in the width direction.

Combining with the contact patch length model [30], the pressure values corresponding to any width position are input into the model to calculate the corresponding contact patch length at that position.

$$a(v) = a_1\frac{Q_{zy}(v)^{a_2}}{P^{a_3}} \tag{11}$$

where a_1 is the constant coefficient of half-length of contact patch, a_2 is the load coefficient of half-length of contact patch, and a_2 is the pressure coefficient of half-length of contact patch.

In the absence of slip, there is no bias in the pressure distribution function along the longitudinal direction; thus, Δ_x equals 0. Simultaneously, regarding the direction of length of contact patch, the concavity and convexity of the pressure distribution function align with the analysis of the direction of width of the contact patch, influenced by both load and

tire pressure. The specific expression for the two-dimensional ground pressure distribution function is as follows:

$$u = \frac{x}{a(v)} \tag{12}$$

$$Q_{zx}(u,v) = \frac{Q_{zy}(v)}{2a(v)}\eta_x(u) \tag{13}$$

$$\eta_x(u) = A_x\left(1-u^2\right)\left(1+\lambda_x u^2\right) \tag{14}$$

$$\lambda_x = q_{x1}q_{zy}(v) + q_{x2}P + q_{x3} \tag{15}$$

$$A_x = \frac{15}{2(5+\lambda_x)} \tag{16}$$

where u is the relative position coordinate along the contact patch lengthwise direction, λ_x is the concavity–convexity factor along the lengthwise direction, q_{x1} is the load coefficient of the lengthwise concavity–convexity factor, q_{x2} is the tire pressure coefficient of the lengthwise concavity–convexity factor, and q_{x3} is the constant coefficient of the lengthwise concavity–convexity factor.

Figure 8 illustrates the pressure distribution obtained through finite element simulation under a load of 5000 N and a tire pressure of 240 kPa, alongside the results of the two-dimensional pressure distribution model. It can be observed that the established two-dimensional pressure distribution model under camber conditions can describe the trend of pressure distribution under camber conditions and can calculate the pressure value at any point on the contact patch.

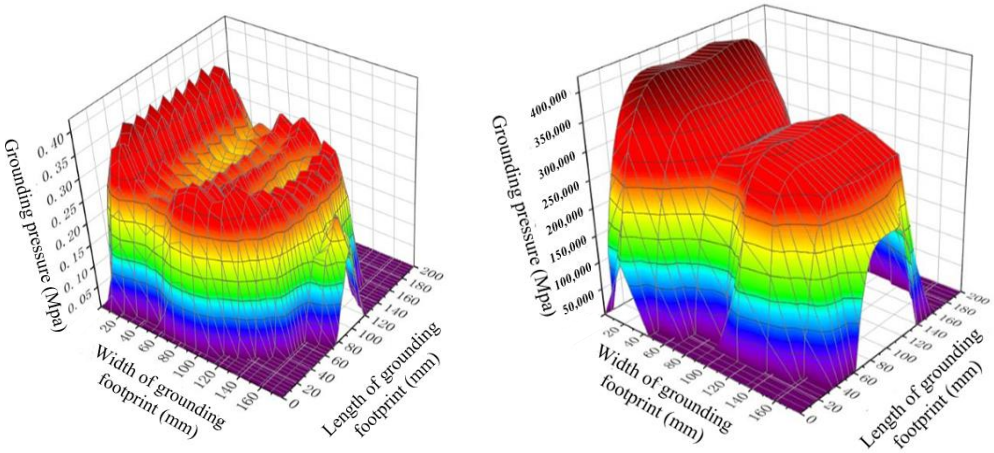

(**a**) (**b**)

Figure 8. Ground pressure distribution at 5000 N and 180 kPa: (**a**) result of finite element model and (**b**) result of ground pressure model.

3.2. Modeling of Camber Brush Model

Figure 9 shows the deformation of the bristles within the tire footprint during camber. Under the influence of tire camber angle, the projection of the tire's belt layer within the footprint can be regarded as a parabola [27]. $y_{\max 0}$ represents the maximum lateral deformation of the bristles at a 0° camber angle, $y_{\max R}$ shows the position of the maximum lateral deformation of the bristles under the influence of a negative camber angle, and $y_{\max L}$ denotes the position of the maximum lateral deformation of the bristles under the influence of a positive camber angle. When the sideslip angle is positive and camber angle is negative, the pressure distribution caused by sideslip in the width direction is consistent with the direction of the pressure distribution caused by the camber [31]. Assuming that after the tire camber the pressure bias caused by sideslip is minimal, it can be neglected.

Consequently, the pressure distribution attributable to camber is utilized to characterize the pressure distribution scenario under conditions of tire camber.

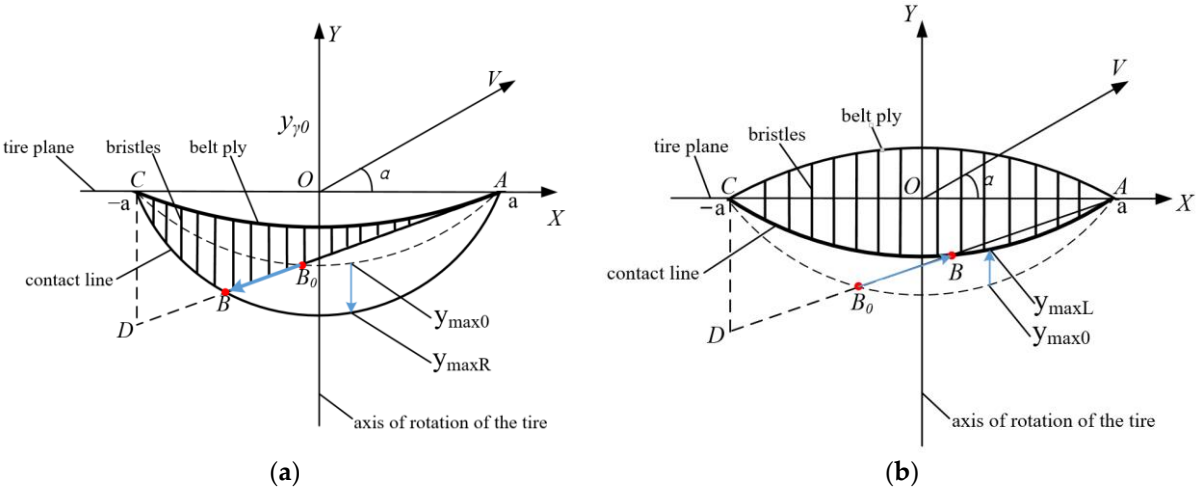

Figure 9. The schematic diagram of camber brush tire model under the influence of camber: (**a**) tire footprint with camber angle effect and (**b**) tire footprint without camber angle effect.

The line segment AC in Figure 10 is the deformation position of the bristles under tire camber. The line segment ABC is the intersection between the lower end of the bristles and the road surface, where AB is the adhesion zone and BC is the slip zone. The region between AC and ABC is the lateral deformation of the bristles. When the tire is cambered, it is common to consider the lateral force F_y generated by camber and the lateral force caused by sideslip as the superposition of lateral force $F_{y\alpha}$ and camber lateral force $F_{y\gamma}$, as shown in Figure 9.

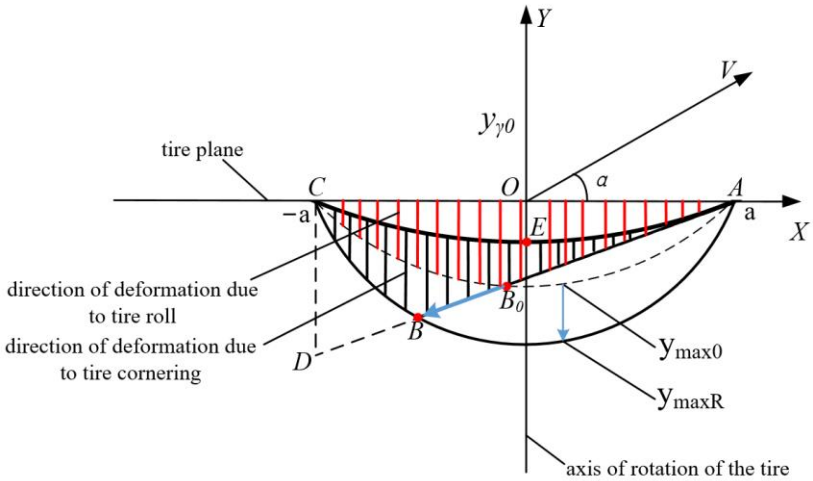

Figure 10. Diagram of lateral force of tire under camber.

The black fine bristle area OAB_0O is the brush deformation under no camber angle and sideslip angle α, with B_0 being the slip point. When there is camber, the brush deformation is represented by the red solid thick brush area $EABCE$. F_y can be approximated as the superposition of two parts: one part is the red solid thick brush area $OABCO$, which is the brush deformation caused by camber under sideslip, with its lateral force denoted as $F_{y\alpha}$, and the other part is the red hollow thick brush area $OAECO$, which is the

brush deformation caused by camber, with its lateral force denoted as $F_{y\gamma}$. Therefore, the expression for lateral force under camber influence is as follows:

$$F_y = F_{y\alpha} + F_{y\gamma} \tag{17}$$

The lateral deformation of the bristles in the adhesion area is as follows:

$$\Delta_y = (a - x)S_y + y_{r0} \tag{18}$$

where S_y is the slip ratio, and y_{r0} is the lateral deformation caused by tire camber.

This lateral deformation is approximately distributed parabolically, and its expression is as follows:

$$y_{\gamma 0} = -\frac{a^2 - x^2}{2R_e}\sin\gamma \tag{19}$$

where R_e is the effective radius.

The lateral force within the adhesion zone is obtained by integration:

$$F_y = \int_a^{x_c} k_{ty}(a - x)S_y dx = K_y S_y - K_{y\gamma}\sin\gamma \tag{20}$$

where $K_{y\gamma}$ is the camber stiffness and sets it to $\frac{2a^3 k_{ty}}{3R_e}$. The relative position horizontal coordinate u_c of the slip point x_c can be obtained from the following equation:

$$k_{ty}\Delta_y(u_c) = \mu_y \frac{F_z}{2a}\eta(u_c) \tag{21}$$

Therefore, the expression for the lateral force under the combined condition of camber and side slip is as follows:

$$\begin{aligned} F_y &= \int_{-a}^{x_c} \frac{\mu_y F_z}{2a}\eta\left(\frac{x}{a}\right)dx + \int_{x_c}^{a} k_{ty}\Delta_y dx \\ &= \frac{(1-u_c)^2}{4}K_y S_y + \frac{1}{2}m_0(u_c)\mu_y F_z - \frac{2 - 3u_c + u_c^2}{4}K_{y\gamma}\sin\gamma \end{aligned} \tag{22}$$

At different width positions of the tire, the contact patch is divided into $2N$ segments along the circumference, and the mechanical characteristics of each segment can be described using a brush tire model. The entire tire is considered to be composed of $2N$ brush models fitted together. Under the effect of camber angle, the contact patch length, vertical load, effective radius, and pressure distribution of each tire segment change. Additionally, assuming that the lateral stiffness and longitudinal stiffness are also divided into $2N$ parts, the specific expression for the load of the i-th brush model segment is as follows:

$$F_z(i) = \frac{F_z}{2N}\eta_y\left(\frac{i}{N}\right), i \in (-N, N) \tag{23}$$

Therefore, the pressure distribution function in the width direction is as follows:

$$\begin{gathered} \eta_y\left(\tfrac{i}{N}\right) = A_y \cdot \left(1 - \left(\tfrac{i}{N}\right)^2\right) \cdot \left(1 + \lambda_y \cdot \left(\tfrac{i}{N}\right)^2\right) \cdot \left(1 - B_y\left(\tfrac{i}{N}\right)\right) \\ \lambda_y = q_{y4} \cdot F_z + q_{y5} \cdot P + q_{y6} \\ A_y = \tfrac{15}{2(5+\lambda_y)} \\ B_y = \tfrac{7(5+\lambda_y)}{7+3\lambda_y} \cdot \tfrac{\Delta_y}{b} \\ \Delta_y = sign(\gamma) \cdot q_{y7} \cdot |\gamma|^{q_{y8}} \end{gathered} \tag{24}$$

where q_{y4} is the load coefficient of concavity–convexity factor in the width direction, q_{y5} is the tire pressure coefficient of concavity–convexity factor in the width direction, and q_{y6} is the constant coefficient of concavity–convexity factor in the width direction.

The expression for the effective radius of the i-th brush model is as follows:

$$R_e(i) = c_1 \frac{P^{c_2}}{F_z(i)^{c_3}} \tag{25}$$

Substituting Equation (25) into the expressions for the relative longitudinal and lateral slip rates yields the following:

$$\begin{aligned} \varphi(i) &= \sqrt{\varphi_x(i)^2 + \varphi_y(i)^2} \\ \varphi_x(i) &= \frac{K_x S_x(i)}{\mu_x F_z(i)} = \frac{K_x}{\mu_x F_z(i)} \cdot \frac{\omega R_e(i) - V_x}{\omega R_e(i)} \\ \varphi_y(i) &= \frac{K_y S_y(i)}{\mu_y F_z(i)} = \frac{K_y}{\mu_y F_z(i)} \cdot \frac{V_y}{\omega R_e(i)} \end{aligned} \tag{26}$$

where $\varphi(i)$ is the comprehensive slip ratio, $\varphi_x(i)$ is the relative longitudinal slip ratio, and $\varphi_y(i)$ is the lateral slip ratio.

The expression for the contact patch length is as follows:

$$a(i) = a_1 \frac{F_z(i)^{a_2}}{P^{a_3}} \tag{27}$$

Substituting the expression for the comprehensive slip ratio allows us to obtain the coordinates of the starting slip point $u_c(i) = i/N$ and the first moment of the pressure distribution function $m_0(u_c(i))$:

$$\begin{gathered} \varphi(i) = \frac{A_x(1 - u_c(i)^2) \cdot (1 + \lambda_x \cdot u_c(i)^2)}{1 - u_c(i)} \\ m_0(u_c(i)) = \int_{-1}^{u_c(i)} A_x(1 - u_c(i)^2) \cdot (1 + \lambda_x \cdot u_c(i)^2) du \\ \lambda_x = q_{x4} \cdot F_z(i) + q_{x5} \cdot P + q_{x6} \\ A_x = A_x = \frac{15}{2(5 + \lambda_x)} \end{gathered} \tag{28}$$

By substituting the ground contact length, normal load, effective radius, and pressure distribution function of each tire segment into the final formula for determining the lateral force under tire camber condition, we can obtain the longitudinal force and lateral force of any tire model segment:

$$\begin{aligned} F_x(i) &= \frac{(1-u_c(i))^2}{4} \cdot K_x(i) S_x(i) + \mu_x F_z(i) \frac{\varphi_x(i)}{\varphi} \cdot \frac{m_0(u_c(i))}{2} \\ F_y(i) &= \frac{(1-u_c(i))^2}{4} K_y(i) S_y(i) + \mu_y F_z(i) \frac{m_0(u_c(i))}{2} - \frac{2 - 3u_c(i) + u_c(i)^2}{4} K_{y\gamma} \sin\gamma \end{aligned} \tag{29}$$

The total lateral force and total longitudinal force in the tire contact area are given by the following:

$$\begin{aligned} F_x &= \sum_{i=1}^{2N} F_x(i) \\ F_y &= \sum_{i=1}^{2N} F_y(i) \end{aligned} \tag{30}$$

Figure 11 presents the simulation results of longitudinal and lateral forces of the brush model under combined lateral slip and longitudinal slip conditions at 6000 N, along with the corresponding experimental data [32]. It can be observed that the simulation results of the theoretical model generally describe the overall trends accurately. With the increase in longitudinal slip ratio, the longitudinal force exerted on the tire gradually increases under different lateral slip angles, showing a stable trend under large slip conditions; the lateral force curve of the model exhibits a nearly symmetrical distribution.

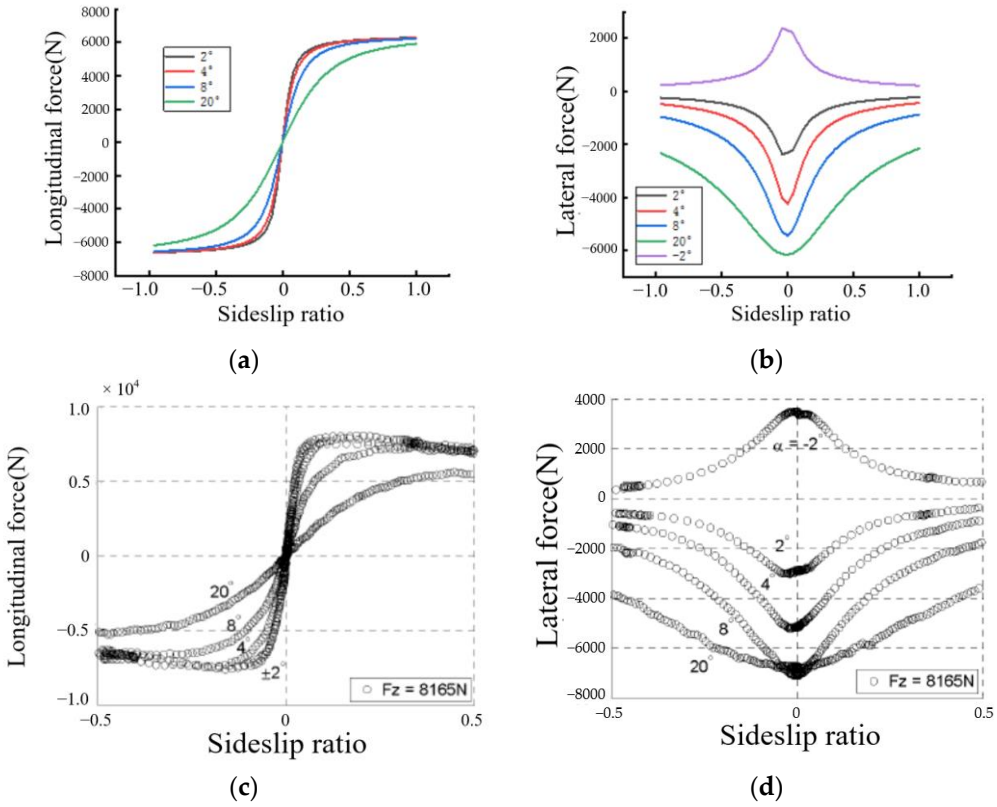

Figure 11. Model and experimental results comparison: (**a**) simulated longitudinal force, (**b**) simulated lateral force, (**c**) experimental longitudinal force, and (**d**) experimental lateral force.

4. Estimation of Road Adhesion Coefficient

In recent years, significant advancements have been made in vehicle dynamics control technology. Liang et al. [33] proposed a distributed control architecture integrating Active Front Steering (AFS) and Direct Yaw Control (DYC), achieving coordination among control systems through the Pareto optimal theory. This control strategy significantly enhances vehicle lateral stability and reduces driver workload during path tracking. Lu et al. [34] developed a high-fidelity CarSim vehicle model embedded with a driver simulator to collect driver data, based on which they defined normalized steering angle input and collision time to quantify driving performance. Zheng [35] proposed a hierarchical extenics coordination controller that considers the bounded rationality of control systems to address the interference of traditional stability control on driving speed and driver operations. This section integrates vehicle dynamics with the improved tire brush model to enhance the accuracy of adhesion coefficient estimation under complex conditions.

In the preceding sections, the constructed tire camber brush model effectively captures the mechanical characteristics of the tire contact patch area (such as the vertical pressure distribution, *Fz*). In this section, a seven-degree-of-freedom vehicle dynamics model is established, with the tire mechanics calculation module adopting the constructed camber brush model. The primary purpose of this integration is to more accurately simulate the driving behavior of electric vehicles under various road and driving conditions. By considering the camber angle and vehicle dynamics characteristics, we are able to describe the tire–road contact more accurately, thus enhancing the accuracy of adhesion coefficient estimation. Furthermore, an estimation of road adhesion coefficient is conducted using an extended Kalman filter-based method, which dynamically adjusts the coefficient based on real-time measurement data, further enhancing estimation precision.

4.1. Definition of Road Adhesion Coefficient

The maximum value of the interaction force between the tire and the ground is known as the adhesion force of the tire to the ground, denoted as F_μ, as shown in the following equation. From the expression, it can be seen that the tire's vertical load is directly proportional to the adhesion force, with the proportionality constant μ being the road adhesion coefficient:

$$F_\mu = \mu \cdot F_z \tag{31}$$

According to theories related to the brush tire model and vehicle dynamics, the road surface adhesion coefficient μ is the coefficient of friction between the tire in static load or pure sliding states and the road surface, reflecting the most fundamental friction properties between the tire and the road surface. Additionally, the friction force from the ground to the tire, which is the tire force in the tire model, forms one of the bases for vehicle dynamics analysis. Therefore, in calculations, the tire force F is constrained not to exceed the adhesion limit, as described by the following formula:

$$F \leq F_\mu = \mu \cdot F_z \tag{32}$$

4.2. Seven-Degree-of-Freedom Vehicle Dynamics Model

Given the direct influence of tire conditions on estimating the road adhesion coefficient, a seven-degree-of-freedom vehicle dynamics model is established, taking into account the longitudinal, lateral, and yaw motions of the vehicle as well as the rotation of all four wheels. As shown in Figure 12, the vehicle's center of gravity is the origin of the coordinate system, with the longitudinal axis of the car as the x-axis, and leftward movement during forward motion is considered positive; moreover, torque within the horizontal plane is deemed positive in the counterclockwise direction. Additionally, the following assumptions are made for the established vehicle dynamics model:

(1) The influence of aerodynamic drag on vehicle dynamics is disregarded;
(2) Vertical bouncing of the vehicle, as well as the whole vehicle's pitch and tilting motions, are not considered;
(3) It is assumed that the physical characteristics of all four tires are identical.

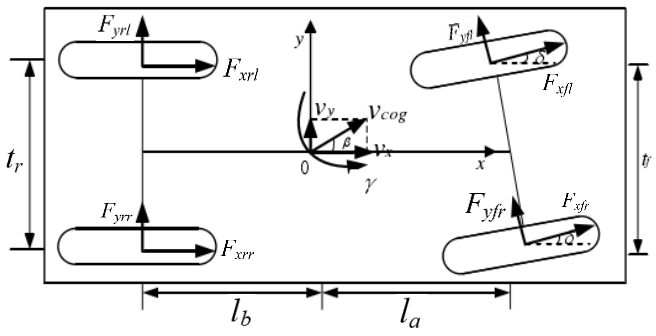

Figure 12. Seven-degree-of-freedom vehicle model.

The dynamic equations of the vehicle are as follows:
Longitudinal motion equation:

$$\begin{gathered} \dot{v}_x = a_x + v_y \cdot \gamma v_x \\ a_x = \frac{1}{m}(F_{xfl}\cos\delta + F_{xfr}\cos\delta + F_{xrl} + F_{xrr} - F_{yfl}\sin\delta - F_{yrl}\sin\delta) \end{gathered} \tag{33}$$

Lateral motion equation:

$$\begin{gathered} \dot{v}_y = a_y + v_x \cdot \gamma \\ a_y = \frac{1}{m}(F_{xfl}\sin\delta + F_{xfr}\sin\delta + F_{yfl}\cos\delta + F_{yfr}\cos\delta + F_{yrl} + F_{yrr}) \end{gathered} \tag{34}$$

Yaw motion equation:

$$\begin{gathered}\dot{\gamma} = \frac{1}{I_z} \cdot \Gamma \\ \Gamma = l_a(F_{xfl} + F_{xfr}) \sin\delta + l_a(F_{yfr} + F_{yfl}) \cos\delta - l_b(F_{yrl} + F_{yrr}) \\ -\frac{t_f}{2}(F_{xfl} - F_{xfr}) \cos\delta + \frac{t_f}{2}(F_{yfl} - F_{yfr}) \sin\delta - \frac{t_r}{2}(F_{xrl} - F_{xrr})\end{gathered} \tag{35}$$

Wheel rotation equation:

$$\begin{gathered}J\dot{w}_{fl,fr} = T_{dfl,fr} - T_{bfl,fr} - T_{xf,fr}R \\ J\dot{w}_{rl,rr} = F_{xrl,rr}R - T_{brl,rr}\end{gathered} \tag{36}$$

The physical meanings of the parameters represented by each symbol are shown in Table 4, where subscripts f and r denote front and rear axles, and r and l denote right and left sides, respectively.

Table 4. Physical significance of each parameter.

Parameter	Physical Significance	Parameter	Physical Significance
v_x	Vehicle longitudinal speed	v_y	Vehicle lateral speed
a_x	Longitudinal acceleration	a_x	Lateral acceleration
γ	Yaw rate	δ	Front tire angle
m	Vehicle mass	I_z	Inertia of rotation around the z-axis
Γ	Yaw moment around the z-axis	t_f	Front tread
t_r	Rear tread	F_{xij}	Longitudinal force
F_{yij}	Lateral force	J	Tire rotational inertia
R	Tire cambering radius	$w_{i,j}$	Tire angular acceleration
$T_{di,j}$	Tire driving torque	$T_{bi,j}$	Tire braking torque

4.3. Estimation of Road Adhesion Coefficient Based on Extended Kalman Filter

4.3.1. Establishment of Systematic Measurement Equations

The established measurement equation is given in the following equation:

$$y(t) = h(x_p(t), u(t), v(t)) \tag{37}$$

where $x_p(t)$ is the parameter to be estimated; $y(t)$ is the measurement output; $u(t)$ is the control input; and $v(t)$ is the observation noise. The parametric variable $x_p(t) = [\mu_1\ \mu_2\ \mu_3\ \mu_4]^T$; the measurement variable $y = \left[a_x\ a_y\ \Gamma\right]^T$; the control input $u = [\delta]$.

4.3.2. Linearization of the Model

In the following equation, *H(t)* denotes the Jacobi matrix of the nonlinear function with *h(x_P(t),u(t),v(t))* partial derivatives for each parameter.

$$H(t) = \begin{bmatrix} \frac{\partial h_1}{\partial x_{p1}}, \ldots, \frac{\partial h_1}{\partial x_{pn}} \\ \ldots\ldots\ldots\ldots\ldots \\ \frac{\partial h_m}{\partial x_{p1}}, \ldots, \frac{\partial h_m}{\partial x_{pn}} \end{bmatrix} \tag{38}$$

$$H(t) = \begin{bmatrix} \frac{F_{x\_fl} - F_{y\_fl}\delta}{m} & \frac{F_{x\_fr} - F_{y\_fr}\delta}{m} & \frac{F_{x\_rl}}{m} & \frac{F_{x\_rr}}{m} \\ F_{x\_fl}\delta + F_{y\_fl} & F_{x\_fr}\delta + F_{y\_fr} & F_{y\_rl} & F_{y\_rr} \\ H(3,1) & H(3,2) & H(3,3) & H(3,4) \end{bmatrix} \tag{39}$$

$$\begin{gathered}H(3,1) = \frac{a(F_{x\_fl}\delta + F_{y\_fl})/I_z + T_f/2(F_{x\_fl} - F_{y\_fl}\delta)}{I_z} \\ H(3,2) = \frac{a(F_{x\_fr}\delta + F_{y\_fr}) - T_f/2(F_{x\_fr} - F_{y\_fr}\delta)}{I_z} \\ H(3,3) = \frac{-(bF_{y\_rl} - T_r/2F_{x\_rl})}{I_z} \\ H(3,4) = \frac{-(bF_{y\_rr} + T_r/2F_{x\_rr})}{I_z}\end{gathered} \tag{40}$$

4.3.3. Implementation of the Recursive Algorithm

The specific workflow of the EKF filtering algorithm is shown in Figure 13. In Figure 13, Q is the covariance matrix of the system excitation noise $w(t)$, and R is the covariance matrix of the measurement noise $v(t)$.

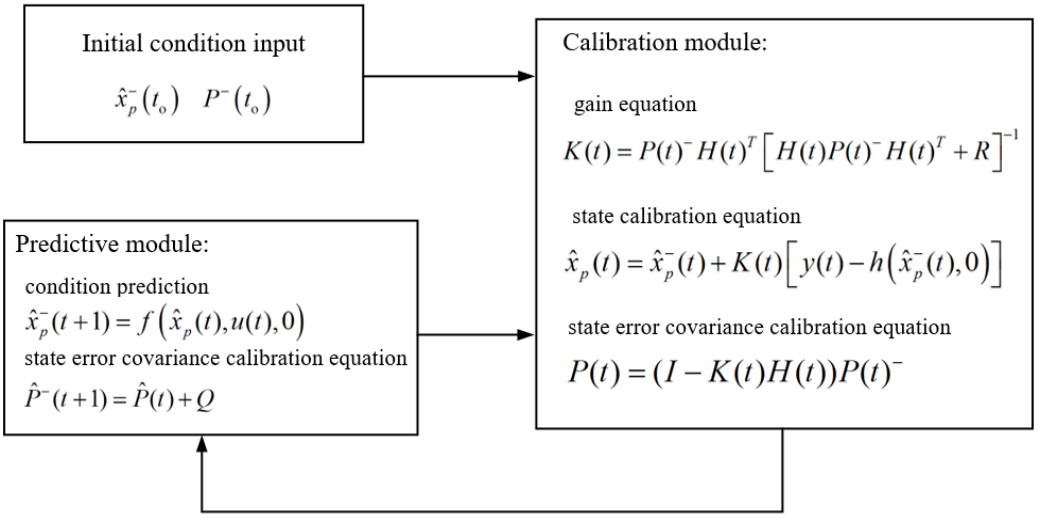

Figure 13. EKF algorithm framework.

4.4. Model Simulation Result Analysis

To verify the performance of the established road adhesion coefficient identification algorithm, two road conditions were simulated. One is dry asphalt road with good adhesion conditions, and the other is waterlogged road with poor adhesion conditions, with road friction coefficients of 0.8 and 0.3, respectively. The left front and rear tire camber angle were set to 3° and 6°, while the right was set to −3° and −6°.

Figure 14 illustrates the estimation results on low-adhesion road surfaces. (a) depicts the estimation of road adhesion coefficient when tire camber angle is 0°. From the figure, it can be observed that the estimated value begins to converge to approximately 0.3045 at around 0.12 s, with a relative error of 1.5% compared to the true value. (b) shows the scenario with a tire camber angle of 3°, where the adhesion coefficient estimate starts to converge to about 0.3057 at around 0.5 s, with a relative error of 1.9%. However, the convergence speed is slower. (c) illustrates the case with a camber angle of 6°, where the adhesion coefficient estimate begins to converge to around 0.3084 at approximately 0.5 s, with a relative error of 2.8%.

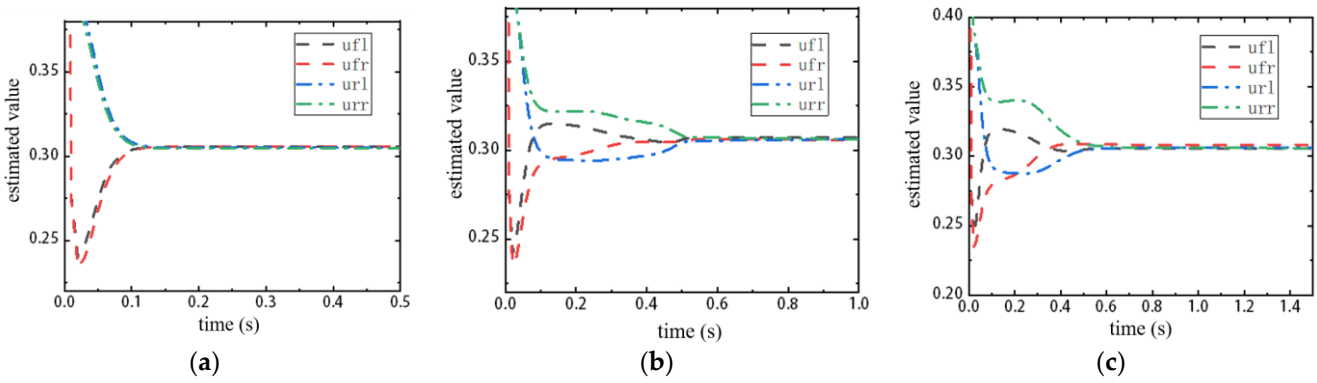

Figure 14. Estimation results of low adhesion road surfaces: (**a**) estimated adhesion coefficients at 0° tire roll angle, (**b**) at 3° tire roll angle, and (**c**) at 6° tire roll angle.

Figure 15 is the estimation results on high-adhesion road surfaces. (a) shows the estimation results of road surface adhesion coefficients for all four wheels when tire camber angle is 0°. It can be observed from the figure that the estimated adhesion coefficient starts converging around 0.14 s to approximately 0.8127–0.8142, with a relative error of 1.58–1.78% compared to the true value. In (b), with a tire camber angle of 3°, the estimated adhesion coefficient begins to converge around 0.5 s to the range of approximately 0.8167–0.8193, with a relative error ranging from 2.09% to 2.33%. As shown in (c), for a tire camber angle of 6°, the estimated adhesion coefficient starts converging around 0.7 s to around 0.819–0.823, with a relative error ranging from 2.3% to 2.86%.

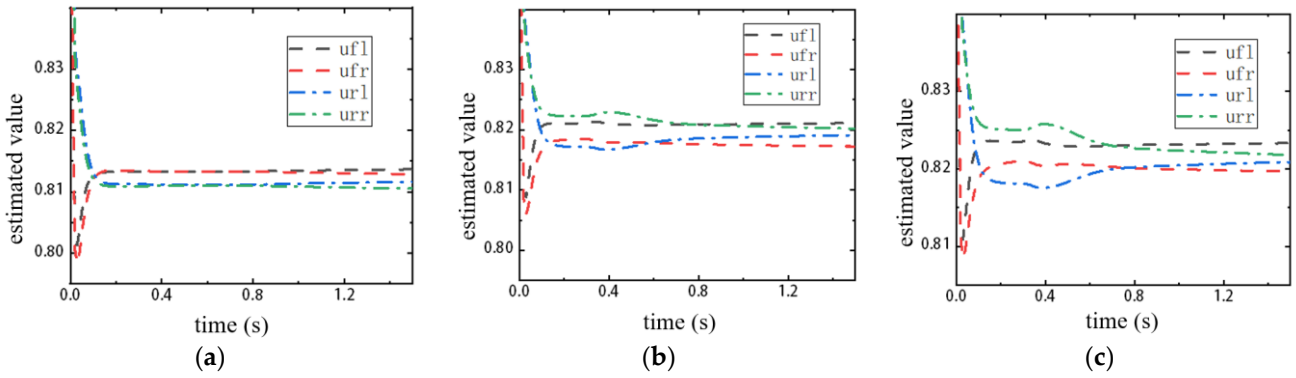

Figure 15. Estimation results of high adhesion road surfaces: (**a**) estimated adhesion coefficients at 0° tire roll angle, (**b**) at 3° tire roll angle, and (**c**) at 6° tire roll angle.

The road surface adhesion coefficient estimation results under high-adhesion road conditions, with the tire model replaced by the original tilt brush tire model, are illustrated in Figure 16.

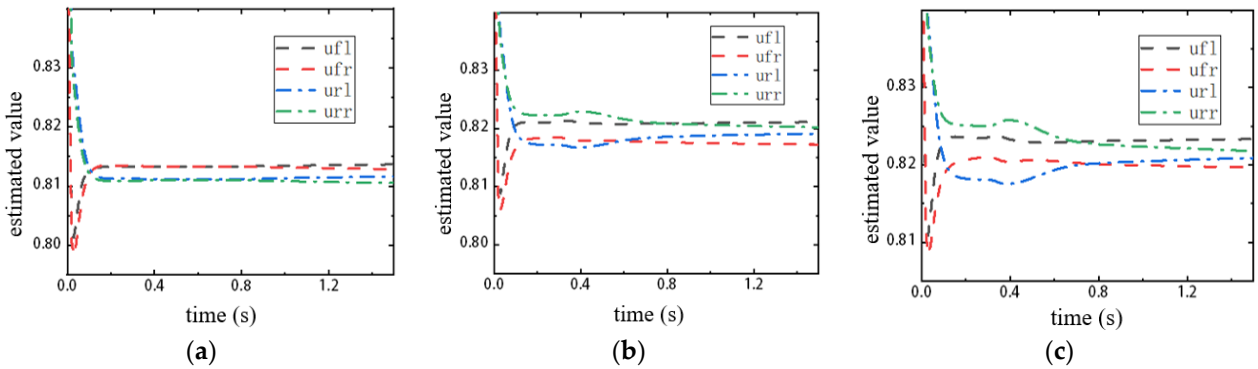

Figure 16. Estimated adhesion coefficients for the pre-improved tire brush model: (**a**) estimated adhesion coefficients at 0° tire roll angle, (**b**) at 3° tire roll angle, and (**c**) at 6° tire roll angle.

The road surface adhesion coefficient estimation results under high-adhesion road conditions, with the tire model replaced by the original tire camber brush tire model, are illustrated in Figure 17.

From Figure 16, it can be observed that, when tire camber angle is 0°, the estimated adhesion coefficient converges to approximately 0.8132–0.8152 at around 0.15 s, with a relative error of 1.65–1.9%. When tire camber angle is 3°, the estimated adhesion coefficient begins to converge to the range of 0.817–0.821 around 0.5 s, with a relative error between 2.12% and 2.62%. At a tire camber angle of 6°, the estimated adhesion coefficient converges to approximately 0.828–0.83 around 0.7 s, with a relative error ranging from 2.86% to 3.76%.

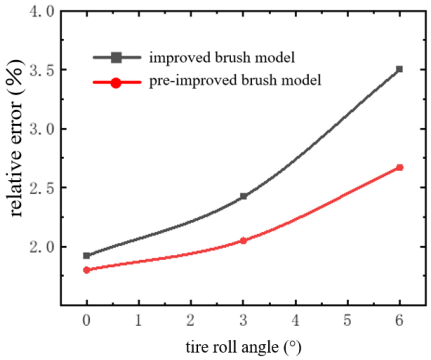

Figure 17. Relative error comparison.

From Figure 17, it can be observed that, when there is no camber angle, the relative error between the adhesion coefficient estimated based on the original and improved brush models is close. This is because when tire camber angle is 0°, the widthwise ground pressure distribution of the tire is symmetric, and the output values of the original and improved tire models are similar. As tire camber angle increases, the relative error between the estimated adhesion coefficient and the true value begins to increase. However, the growth rate of the relative error for the improved brush model is smaller than that of the original brush model, indicating that the improved brush model can better describe the adhesion performance of the tire under camber conditions. Nonetheless, the improved brush model still exhibits some errors in adhesion coefficient estimation. In the research, the sources of relative error in estimating road adhesion coefficient mainly include the following: model simplification and assumptions, sensor noise and measurement inaccuracy, and variation in road conditions. Although the camber brush model has a certain level of accuracy, it simplifies the interaction between tire and road surface. For example, the assumption of uniform pressure distribution does not hold true under all conditions, leading to deviations in estimation results. The accuracy of the extended Kalman filter (EKF) algorithm largely depends on the quality of input data and sensor measurement noise, such as inaccuracies in detecting tire forces and inclination angles, and can lead to estimation errors. Moreover, actual road conditions vary significantly, with factors such as road surface texture, temperature, and humidity affecting tire–road interaction, which are not fully captured in the model.

In summary, the brush model considering the asymmetric ground contact characteristics of the tire demonstrates higher accuracy in estimating the adhesion coefficient compared to the improved brush model. This indicates that the improved brush model can more accurately reflect the mechanical characteristics of the tire under asymmetric ground contact distribution.

5. Conclusions

Tire camber can alter the ground contact characteristics between the tire and the road surface. In this paper, based on the two-dimensional ground pressure distribution model under tire camber conditions, a camber brush tire model considering the influence of tire width was constructed. Combined with the seven-degree-of-freedom vehicle model, the extended Kalman filter algorithm was utilized to estimate the road adhesion coefficient under tilting conditions. According to the analysis of the model simulation results, the main conclusions are as follows:

1. The influence of load on the width of the ground contact patch: under camber conditions, the width of the ground contact patch varies significantly under low loads, while the variation is less pronounced under high loads.
2. The influence of inflation pressure on the width of the ground contact patch: when the tire is under low load, the inflation pressure has a minor effect on the width variation.

However, under high load conditions, a higher inflation pressure leads to a greater variation in the width of the ground contact patch.

3. The influence of load on ground pressure distribution: under tire camber conditions, the smaller the load, the more pronounced the lateral shift of the ground pressure towards the tilted side. Conversely, with larger loads, the overall lateral shift of the ground pressure decreases, and there is an increasing trend of pressure distribution in the central area of the ground contact patch becoming concave.
4. The influence of inflation pressure on ground pressure distribution: under lateral tilt conditions, the lower the inflation pressure, the more pronounced the lateral shift of the ground pressure towards the tilted side. Conversely, with higher inflation pressure, the lateral shift of the ground pressure towards the tilted side decreases, and there is an increasing trend of pressure distribution in the central area of the ground contact patch becoming convex.
5. The optimized tire brush model constructed in this study integrates a two-dimensional ground contact pressure distribution model under camber conditions, effectively accounting for the asymmetry in ground contact pressure distribution during tire operation. Compared to previous tire models, the optimized tire brush model can be applied to a wider range of conditions and better predicts the mechanical characteristics of the contact area under camber conditions.
6. The constructed road adhesion coefficient estimation model can rapidly and accurately estimate the road adhesion coefficient, demonstrating the effectiveness of the adhesion coefficient estimation algorithm based on the camber brush model. This also indirectly validates the effectiveness of the camber tire model.

Author Contributions: Conceptualization, S.Z. and H.Z. (Hongcheng Zhu); methodology, S.Z. and H.Z. (Hongcheng Zhu); software, H.Z. (Hongcheng Zhu) and Y.L.; validation, S.Z., H.Z. (Hongcheng Zhu) and Y.C.; formal analysis, H.Z. (Hongcheng Zhu); resources, Y.C. and Y.L.; writing—original draft preparation, H.Z. (Hongcheng Zhu); writing—review and editing, S.Z. and H.Z. (Hongcheng Zhu); funding acquisition, S.Z. and H.Z. (Haichao Zhou). All authors have read and agreed to the published version of the manuscript.

Funding: This research was funded by "The National Natural Science Foundation of China, grant number 52072156".

Data Availability Statement: Data are contained within the article.

Conflicts of Interest: The authors declare no conflicts of interest.

References

1. Zhang, S.; Liu, Y.; Zhou, H.; Zhang, W.; Chen, Y.; Zhu, H. Analysis of the Effect of Wear on Tire Cornering Characteristics Based on Grounding Characteristics. *World Electr. Veh. J.* **2023**, *14*, 166. [CrossRef]
2. Han, Y.; Lu, Y.; Chen, N.; Wang, H. Research on the Identification of Tyre-Road Peak Friction Coefficient under Full Slip Rate Range Based on Normalized Tyre Model. *Actuators* **2022**, *11*, 59. [CrossRef]
3. Timmers, V.R.; Achten, P.A. Non-exhaust PM emissions from electric vehicles. *Atmos. Environ.* **2016**, *134*, 10–17. [CrossRef]
4. Lee, H.; Taheri, S. Intelligent tires a review of tire characterization literature. *IEEE Intel. Transp. Sy.* **2017**, *9*, 114–135. [CrossRef]
5. Liu, C.-S. Adhesion coefficient of automobile tire and road surface. *J. Central South. Univ. Technol.* **2008**, *15*, 210–214. [CrossRef]
6. Andersson, M.; Bruzelius, F.; Casselgren, M.; Gafvert, M.; Hjort, M.; Hulten, J.; Habring, F.; Klomp, M.; Olsson, G.; Sjodahl, M.; et al. *Road Friction Estimation*; Intelligent Vehicle Safety Systems: Gothenburg, Sweden, 2007.
7. Alonso, J.; López, J.; Pavón, I.; Recuero, M.; Asensio, C.; Arcas, G.; Bravo, A. On-board wetroad surface identification using tyre/road noise and support vector machines. *Appl. Acoust.* **2014**, *76*, 407–415. [CrossRef]
8. Khaleghian, S. *The Application of Intelligent Tires and Model Based Estimation Algorithms in Tire-Road Contact Characterization*; Virginia Polytechnic Institute and State University: Blacksburg, VA, USA, 2017.
9. Arto, J.; Niskanen Ari, J. Tuononen. Three 3-axis accelerometers fixed inside the tyre for studying contact patch deformations in wet conditions. *Veh. Syst. Dyn.* **2014**, *52* (Suppl. 1), 287–298.
10. Gustafsson, F. Monitoring tire-road friction using the wheel slip. *Control. Syst. IEEE* **1998**, *18*, 42–49.
11. Alexander, L.; Rajamani, R. Tire road friction coefficient estimation. *J. Dyn. Syst. Meas. Control* **2004**, *126*, 265–275.
12. Bergman, W.; Clemett, H.R. Tire cornering properties. *Tire Sci. Technol.* **1975**, *3*, 135–163. [CrossRef]
13. Fiala, E. Seitenkrafte am rollenden luftreifen (Lateral forces on rolling pneumatic tires). *Zeitschrift V. D. I.* **1954**, *96*, 973–979.

14. Frank, F. Grundlagen zur berechnung der seitenfuhrungskennlinien von reifen. *Kautschunk Unt Qummi* **1965**, *8*, 267–274.
15. Duggff, H.; Fancher, P.; Segel, L. *An Analysis of Tire Traction Properties and Their Influence on Vehicle Dynamics Performance*; International Automobile Safety Conference Compendium, Society of Automotive Engineers: New York, NY, USA, 1970.
16. Bakker, E.; Nyborg, L.; Pacejka, H.B. Tyre modeling for use in vehicle dynamics studies. *SAE Tech. Pap.* **1987**, *870421*, 190–204.
17. Sakai, H. Study on cornering properties of tire and vehicle. Tire Science and Technology. *TSTCA* **1990**, *18*, 136–139.
18. Kuiper, E.; Van oostenjj, M. The PAC2002 advanced handling tire model. *Veh. Syst. Dyn.* **2007**, *45*, 153–167. [CrossRef]
19. Bai, F.; Guo, K.; Lu, D. Tire model for turn slip properties. *SAE Int. J. Commer. Vehicles.* **2013**, *6*, 353–361. [CrossRef]
20. Su, X.; Fu, P.; Ding, Z.; Li, D.W.; Yang, M.F. Establishment and Simulation Analysis of Tire Finite Element Model Based on Abaqus Software. *China Rubber Ind.* **2019**, *66*, 121–127.
21. Han, Y. Research on the Peak Adhesion Coefficient Estimation of Three-Dimensional Road Based on Normalized Tire Model. Ph.D. Thesis, Shijiazhuang Tiedao University, Shijiazhuang, China, 2022.
22. Mendoza-Petit, M.F.; García-Pozuelo, D.; Díaz, V.; Olatunbosun, O. A Strain-Based Intelligent Tire to Detect Contact Patch Features for Complex Maneuvers. *Sensors* **2020**, *20*, 1750. [CrossRef] [PubMed]
23. He, H.; Li, R.; Yang, Q.; Pei, J.; Guo, F. Analysis of the tire-pavement contact stress characteristics during vehicle maneuvering. *Ksce J. Civ. Eng.* **2021**, *25*, 2451–2463. [CrossRef]
24. Zheng, B.; Chen, J.; Zhao, R.; Tang, J.; Tian, R.; Zhu, S.; Huang, X. Analysis of contact behaviour on patterned tire-asphalt pavement with 3-D FEM contact model. *Int. J. Pavement Eng.* **2022**, *23*, 171–186. [CrossRef]
25. Yu, L.; Hu, J.; Li, R.; Yang, Q.; Guo, F.; Pei, J. Tire-pavement contact pressure distribution analysis based on ABAQUS simulation. *Arab. J. Sci. Eng.* **2022**, *47*, 4119–4132. [CrossRef]
26. Yadav, R.; Raheman, H. Development of an artificial neural network model with graphical user interface for predicting contact area of bias-ply tractor tyres on firm surface. *J. Terramech.* **2023**, *107*, 1–11. [CrossRef]
27. Li, X.; Xu, N. Effect of inflation pressure on tyre forces under combined-slip conditions based on the UniTire model. *Int. J. Veh. Des.* **2023**, *91*, 322–341. [CrossRef]
28. Systèmes, D. *SIMULIA User Assistance 2020*; Abaqus: Providence, RI, USA, 2020.
29. Chen, X. Research on Numerical Analysis Method and Evaluation Index of Wet Grip Performance of Tire. Master's Thesis, Jiangsu University, Zhenjiang, China, 2019.
30. Zhang, B.; Xu, T.; Wang, H.; Huang, Y.; Chen, G. Vertical Tire Forces Estimation of Multi-Axle Trucks Based on an Adaptive Treble Extend Kalman Filter. *Chin. J. Mech. Eng.* **2021**, *34*, 55. [CrossRef]
31. Chen, G.; Wang, X.; Su, L.; Wang, Y. Safety distance model for longitudinal collision avoidance of logistics vehicles considering slope and road adhesion coefficient. *Proc. Inst. Mech. Eng. J. Automob. Eng.* **2020**, *235*, 498–512.
32. Xu, N. Study on the Steady State Tire Model under Combined Conditions. Ph.D. Thesis, Jilin University, Jilin, China, 2012.
33. Liang, J.; Lu, Y.; Yin, G.; Fang, Z.; Zhuang, W.; Ren, Y.; Xu, L.; Li, Y. A Distributed Integrated Control Architecture of AFS and DYC based on MAS for Distributed Drive Electric Vehicles. *IEEE Trans. Veh. Technol.* **2021**, *70*, 5565–5577. [CrossRef]
34. Lu, Y.; Liang, J.; Yin, G.; Xu, L.; Wu, J.; Feng, J.; Wang, F. A Shared Control Design for Steering Assistance System Considering Driver Behaviors. *IEEE Trans. Intell. Veh.* **2022**, *8*, 900–911. [CrossRef]
35. Zheng, Z.C.; Zhao, X.; Wang, S.; Yu, Q.; Zhang, H.C.; Li, Z.K.; Chai, H.; Han, Q. Extension coordinated control of distributed-driven electric vehicles based on evolutionary game theory. *Control Eng. Pract.* **2023**, *137*, 105583. [CrossRef]